International Journal of Greenhouse Gas Control 106 (2021) 103217

Contents lists available at ScienceDirect

International Journal of Greenhouse Gas Control

journal homepage: www.elsevier.com/locate/ijggc

Combined geophysical and rock physics workflow for quantitative CO_2 monitoring

Bastien Dupuy [a,*], Anouar Romdhane [a], Peder Eliasson [a], Hong Yan [b]

[a] SINTEF Industry, Norway
[b] NTNU, Norway

ARTICLE INFO

Keywords:
CCS
Monitoring
Monitoring workflow
Uncertainty quantification
Conformance monitoring
Geophysical inversion
Bayesian inversion

ABSTRACT

Safe CO_2 storage requires conformance verification, i.e. confirmation that the pressure and CO_2 accumulation are consistent with modelling forecasts within a given uncertainty range. Quantitative estimates of relevant reservoir parameters (e.g. pore pressure and fluid saturations) are usually derived from geophysical monitoring data (e.g. seismic, electromagnetic and/or gravity data) and potential prior knowledge of the storage reservoir. We describe a two-step strategy combining geophysical and rock physics inversions for quantitative CO_2 monitoring. A Bayesian formulation is used to propagate and account for uncertainties in both steps. We demonstrate our workflow using datasets from the Sleipner CO_2 storage project (Norwegian North Sea) and combining seismic Full Waveform Inversion and rock physics inversion. We derive rock frame properties from baseline data and use them as input to obtain 2D spatial distribution of CO_2 saturation with uncertainty assessment from monitor data. We also discuss the need for advanced rock physics models, considering the way fluid phases are mixed (uniform to patchy mixing) and the trade-off effects of pore pressure and fluid saturation on geophysical measurements. We consequently recommend a joint rock physics inversion approach, where multi-physics, and multi-parameter inversion can be used for better discrimination of pressure, saturation, and fluid mixing effects towards more quantitative conformance verification.

1. Introduction

With increasingly visible effects of climate change and a growing awareness of the possible consequences, Carbon Capture and Storage (CCS) technologies are gaining momentum (IPCC, 2005). Recent studies show that large-scale (gigatonne) CO_2 storage is feasible (Ringrose and Meckel, 2019), and several large-scale CCS projects are now running or are under development (e.g. Sleipner, Quest, Tomakomai, Lula, or Northern Lights/Longship). However, the safety of geological CO_2 storage and whether the CO_2 will stay in the reservoir are questions often raised by policy makers and by the general public. Several arguments support the safety of CO_2 storage (Furre et al., 2019), the three strongest ones being:

- CO_2 storage, and associated monitoring, has been implemented for over 20 years, e.g. in the North Sea at the Sleipner storage site (Eiken et al., 2011; Furre et al., 2017; Eiken, 2019).
- With geophysical monitoring, we can track the CO_2 accumulation in the storage complex and evaluate whether the CO_2 is contained in the reservoir or leaking through the overburden.
- Operators are able to demonstrate conformance with respect to existing regulations (e.g. EU, US, and Norwegian directives (EC, 2011)).

An extended review of the state-of-the-art in CO_2 storage is given by Davis et al. (2019) while Pawar et al. (2015) review advances in risk assessment of an entire CO_2 storage project, i.e. from the pre-injection site characterisation to the post-closure phase. Since the risk assessment is site-specific and contains time-dependent uncertainties, they recommend using probabilistic approaches. They also explain that the CO_2 storage operators are facing increasing requests from policy makers to provide "meaningful quantitative indicators", e.g. leakage rates or spatially anomalous CO_2 saturations.

Measurement, Monitoring and Verification (MMV) programs (Bourne et al., 2014; Dean and Tucker, 2017) play a critical role in evaluating storage performance and assessing the risks associated with

* Corresponding author at: Bastien Dupuy, SINTEF Industry, S. P. Andersens veg 15B, 7031, Trondheim, Norway.
E-mail address: bastien.dupuy@sintef.no (B. Dupuy).

https://doi.org/10.1016/j.ijggc.2020.103217
Received 27 April 2020; Received in revised form 12 November 2020; Accepted 24 November 2020
Available online 24 February 2021

CO_2 storage. MMV plans need to fulfil containment and conformance requirements to ensure safe CO_2 storage during injection and after site closure. The containment monitoring aims at verifying the security of CO_2 storage by the surveillance of plume migration and the early detection of potential leakage. The conformance monitoring should prove that the operator understands the behaviour of the CO_2 in the reservoir, i.e. that there is consistency between the model-based predicted behaviour and the CO_2 accumulation estimated from monitoring data. In addition, contingency plans should provide adequate mitigation measures in case of non-conformance. For reliable conformance verification, the monitoring (from well log measurements or geophysical data) should, in addition to locating the CO_2 plume, provide quantitative information, ideally on both CO_2 saturation and pore pressure, to be compared to reservoir modelling predictions. Pore pressure and its development over time in the reservoir and the overburden is a critical parameter for storage safety and it is also the main limiting factor for large-scale storage of CO_2 (Ringrose and Meckel, 2019). After defining the monitoring tasks (e.g. CO_2 plume migration monitoring, pressure development in the storage complex, seal integrity, injection and legacy wells integrity, etc), a careful and fit-for-purpose selection of the monitoring techniques must be done by the operator. The resulting monitoring plan should offer the best compromise between cost and efficiency.

For example, at Sleipner (Norwegian North Sea), the oldest CO_2 storage site, the containment monitoring is validated using time-lapse seismic methods (Arts et al., 2004). The pressure effects in Sleipner are shown to be negligible due to the large size and large permeability of the Utsira sand aquifer (Chadwick et al., 2012). On the other hand, at the Snøhvit site (Barents Sea), pressure unconformities (i.e. unexpected pressure build-up) have been observed after 3 years of injection and were related to unforeseen reservoir pressure barriers. Mitigation measures have been implemented, including stopping the injection and changing the injection target from the Tubåen formation to the overlying Stø formation (Hansen et al., 2013).

MMV plans heavily rely on sparse geophysical measurements (both in time and space) that must be acquired, processed, and interpreted to evaluate the consistency between modelled forecasts (e.g. fluid flow modelling in the reservoir) and the geophysical monitoring measurements. Such evaluation requires deriving and comparing measurable quantities, i.e. relevant subsurface properties affected by the CO_2 injection. Geophysical methods for CO_2 monitoring include seismic, electromagnetic, electrical and gravimetric surveys, each of them having different sensitivities to subsurface property changes caused by CO_2 injection. For example, injection of supercritical CO_2 in a high-porosity, brine-saturated reservoir creates a large decrease in seismic P-wave velocity due to partial saturation as well as a decrease in density and an increase of resistivity.

Monitoring of CO_2 storage sites with geophysical methods is currently considered as standard and many examples can be found in the literature. At Sleipner, Chadwick and Noy (2010) use a qualitative interpretation of time-lapse seismic to history match the plume top layer migration. Wang et al. (2018) derive detection thresholds of a potential leakage through the primary seal by interpretation of time-lapse seismic data. Roach and White (2018) use a similar approach to track the CO_2 plume migration at the Aquistore storage site while Glubokovskikh et al. (2020) focus on the qualitative identification of a small CO_2 leakage with acoustic inversion of time-lapse seismic data. Grude et al. (2013) apply the approach suggested in Landrø (2001) to the Snøhvit dataset and demonstrate that pressure and saturation effects can be discriminated from Amplitude Versus Offset (AVO) time-lapse data. As a complement to seismic surveys, electrical or electromagnetic surveys may be used to monitor CO_2 storage. Bhuyian et al. (2012) perform an extended sensitivity analysis of the use of CSEM (Controlled-Source ElectroMagnetic) for CO_2 plume monitoring. They show that resistivity anomalies can be detected and constitute a good complement to seismic-based monitoring as the resistivity is more sensitive to changes of saturation than seismic P-wave velocity for high CO_2 saturation levels. Commer et al. (2016) recommend, with examples at Cranfield and Escatawpa sites, to carry out ERT (Electrical Resistivity Tomography) in 3D to avoid 2D approximation related artifacts. Bergmann et al. (2012) also show an application of surface to downhole ERT for CO_2 plume migration at Ketzin.

To verify conformance reliably, quantitative interpretation of geophysical data (estimating rock and fluid properties) is very valuable. Doyen (2007) and Bosch et al. (2010) give a good overview of geostatistical methods for oil and gas reservoir characterisation. Such quantification of reservoir parameters, namely rock and fluid properties (rock facies, porosity, fluid saturation…) are usually carried out from seismic reflectivity data using a combination of AVO inversion and rock physics inversion in sequential or integrated steps (Coléou et al., 2005; Grana, 2016; Azevedo et al., 2019). In this context, sampling algorithms such as MCMC (Markov Chain Monte-Carlo) can be used to evaluate uncertainties associated with the recovered parameters (de Figueiredo et al., 2019b; Fjeldstad and Grana, 2018; Azevedo and Demyanov, 2019). For example, Jullum and Kolbjørnsen (2016) estimate rock physics properties from seismic post-stack reflectivity data by

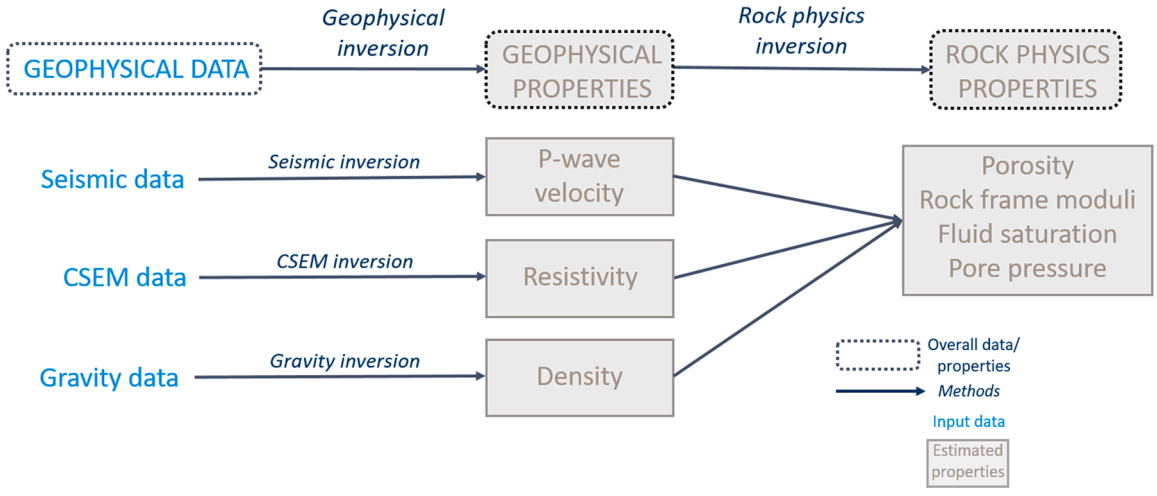

Fig. 1. Generic framework for quantitative monitoring (two-step approach). The top row describes the generic two-step approach with sequential geophysical and rock physics inversions. The bottom rows give specific cases depending on data types that can be run independently or combined in a joint inversion framework. The rock physics properties finally estimated can be different depending on the target and the available data.

linearizing the rock physics model. Using Sleipner AVO data, they derive 1D profiles of CO_2 saturation estimates with uncertainty.

In this paper, we are presenting a generic quantitative approach that considers uncertainties through a Bayesian framework to support conformance verification. The main goal is to obtain estimates (with proper uncertainty assessment) of rock physics properties that (1) can be used to verify conformance, (2) are affected by the CO_2 injection, and (3) have an effect on observed geophysical data. By generic, we mean that our workflow can handle various independent geophysical inversions of seismic, electrical, EM or gravimetric data and gather this information in an integrated second step of joint rock physics inversion. We first introduce the two-step approach for the inversion of geophysical data, combining waveform-based geophysical inversion and rock physics inversion. Then, we discuss the rock physics models linking geophysical observables to rock and fluid properties and the associated sensitivities, especially CO_2 saturation and pore pressure. We finally present examples of the monitoring workflow on the real dataset at Sleipner (focusing on CO_2 saturation), and we discuss how to handle more complex cases and the added value of geophysical data integration.

2. Quantitative inversion approach

Our proposed two-step approach combines geophysical and rock physics inversions for a quantitative characterisation where spatial distributions of selected properties (or property changes) are derived. Geophysical inversions are mainly seismic inversions but other methods like CSEM, ERT and gravity inversion can be used. Recent advances in seismic Full Waveform Inversion (FWI) allow high-resolution mapping of selected geophysical properties of the subsurface directly from the raw data seismograms. Acoustic to visco-elastic approximations of the seismic wave propagation are commonly used to solve the associated forward problem (Virieux and Operto, 2009) with the actual computer resources (Trinh et al., 2018). Some attempts are made to use poroelastic wave propagation theory to have a more realistic representation of the porous medium (De Barros et al., 2010; Morency et al., 2009). However, the inverse problem is highly under-determined and ill-posed, and the computational burden is very large. We consequently choose an alternative approach, splitting the inverse problem into two steps (Dupuy et al., 2016a, b), similarly to the conventional AVO-rock physics inversion approaches (Buland and Omre, 2003; Grana, 2016).

This two-step approach is described in Fig. 1. The first step consists of independent inversions of geophysical data (usually seismic data and possibly additional data such as CSEM, ERT or gravimetric data). The geophysical inversion, usually based on gradient-based local optimization methods, provides a first quantitative parametrization of the subsurface properties such as seismic velocities, densities and/or resistivities. These geophysical properties are then quantitatively "interpreted" as rock physics properties using a second inversion step. This rock physics inversion step aims at combining the different physics (e.g. of seismic and electromagnetic) to derive relevant rock physics properties. For example, P-wave velocity and resistivity are both affected by the porosity and fluid saturations.

3. Bayesian formulation of the two-step inversion approach and uncertainty quantification strategy

Quantification of monitoring parameters must be done with proper uncertainty assessment for reliable conformance verification and associated decision making. A Bayesian formulation (Tarantola, 2005) is appropriate for probabilistic estimations and provides a convenient framework to propagate uncertainty in the two-step inversion approach.

The first step usually requires solving a large-scale, non-linear inverse problem where local or ensemble-based optimization algorithms are used to minimize a distance between modelled and observed data (Virieux and Operto, 2009). The Bayesian inference framework is used to incorporate prior information, uncertainties, and to derive conditional probability distributions of the estimated properties (Fang et al., 2018). In our approach, posterior covariance analysis is the method chosen to assess uncertainty from the first step. The posterior model covariance describes variances of, and covariances between, derived model parameters and is calculated as a reduction of the prior model covariance by the information gained from the geophysical inversion (Duffet and Sinoquet, 2006; Zhu et al., 2016; Eliasson and Romdhane, 2017). The posterior covariance $\boldsymbol{C}_{post}^{FWI}$ from an initial FWI step can be written:

$$\boldsymbol{C}_{post}^{FWI} = \left(\boldsymbol{J}^{\dagger}\boldsymbol{C}_{D_{FWI}}^{-1}\boldsymbol{J} + \boldsymbol{C}_{prior}^{-1}\right)^{-1} \tag{1}$$

where $\boldsymbol{H} = \boldsymbol{J}^{\dagger}\boldsymbol{C}_{D_{FWI}}^{-1}\boldsymbol{J}$ is the Gauss-Newton approximation of the data misfit Hessian. $\boldsymbol{J}$ is the Fréchet derivative of the forward modelling operator with respect to the model parameter vector and $\boldsymbol{J}^{\dagger}$ is its adjoint operator. $\boldsymbol{C}_{D_{FWI}}$ is the data covariance matrix describing seismic data uncertainties while $\boldsymbol{C}_{prior}$ is a prior model covariance. The posterior covariance is estimated using few algebraic reformulations and Singular Value Decomposition (SVD) to exploit the low-rank property of the FWI Hessian (Bui-Thanh et al., 2013). Eliasson and Romdhane (2017) show how the approach allows calculating an ensemble of equivalent models, equally well explaining the observed data, and estimating the posterior variance of the P-wave velocity and resistivity models. Ayani et al. (2020) show that CSEM inversion can be run using stochastic Bayesian inversion formulation for a simple synthetic model (Johansen formation in the North Sea).

For the second step (rock physics inversion), a Bayesian inference framework is also implemented. For example, Grana (2016) and Grana et al. (2017) linearize the rock physics models and derive a Bayesian formulation to estimate rock and fluid properties based on seismic reflection data. Similar probabilistic reservoir characterisation approaches are summed up in the review of Bosch et al. (2010). Dupuy et al. (2019) specifically propose the use of a Bayesian framework to propagate uncertainties derived from the FWI step. The posterior covariance $\boldsymbol{C}_{post}^{FWI}$ is then transformed into a data covariance matrix $\boldsymbol{C}_{D_{RPI}} = \boldsymbol{C}_{post}^{FWI}$. The model $\boldsymbol{m}$ posterior probability density distribution $\sigma_{post}^{RPI}(\boldsymbol{m})$ is formulated such as:

$$\sigma_{post}^{RPI}(\boldsymbol{m}) \propto \rho_{prior}(\boldsymbol{m})\, L\left(\boldsymbol{m}|\boldsymbol{d}\right) \tag{2}$$

with $L(\boldsymbol{m}|\boldsymbol{d})$ being the data likelihood function. Assuming a multidimensional Gaussian distribution, it is described as:

$$L\left(\boldsymbol{m}|\boldsymbol{d}\right) \propto \exp\left[-\frac{1}{2}(\boldsymbol{d} - g(\boldsymbol{m}))^{T} C_{D_{RPI}}^{-1}(\boldsymbol{d} - g(\boldsymbol{m}))\right] \tag{3}$$

The model vector $\boldsymbol{m}$ contains the selected rock physics parameters, e.g. CO_2 saturation, pore pressure and porosity. The observed data vector $\boldsymbol{d}$ contains the input data to the rock physics inversion, e.g. P-wave velocity and resistivity. g is a non-linear rock physics model allowing the computation of geophysical observables (seismic velocities, density, resistivity) from the rock physics parameters (fluid and rock properties). $\rho_{prior}(\boldsymbol{m})$ is a probability density distribution describing prior information about the model parameters. Bayesian inference is by definition a process where the prior distribution is updated to the posterior distribution by making use of the observed information (Tarantola, 2005). The choice of the prior model probability distribution is consequently critical in a Bayesian framework. *A priori* information on rock physics properties is elaborated from well log data, interpreted seismic results, laboratory tests or regional geology knowledge.

Finally, sampling techniques such as Monte-Carlo Markov Chains must be used to get statistically relevant estimation of $\sigma_{post}^{RPI}(\boldsymbol{m})$ (de Figueiredo et al., 2019a, 2019b). Sambridge (1999) combines a first stage to explore the model space efficiently with a neighbourhood algorithm (search stage) with a second stage resampling the ensemble obtained in

the first stage to get a statistical appraisal of the ensemble of models (appraisal stage). An approximation of the posterior probability density function is derived and allows calculation of Bayesian integrals and meaningful estimates of confidence over the model parameters (e.g. posterior probability densities).

4. Rock physics models for CO_2-brine saturated porous media

The rock physics inversion rests upon a calibrated rock physics model. Gassmann-Biot theory (Gassmann, 1951; Biot, 1962) is widely used for fluid substitution problems and is shown to be appropriate for high porosity aquifer sandstones usually encountered in CO_2 storage sites, such as the Utsira sandstone, which is the main reservoir formation of the Sleipner CO_2 storage pilot (Dupuy et al., 2017). We give the complete description of the rock physics model in section 5 and Appendix A. If porosity and rock frame properties are known, e.g. from well log data or baseline inversion, the main parameters affecting the P-wave velocity are the fluid saturations and the fluid properties. The fluid bulk moduli and densities of each phase are derived given the reservoir pressure and temperature conditions of the aquifer. A description of those conditions at Sleipner is provided in Ghaderi and Landrø (2009) and in Furre et al. (2015). The way the two fluid phases are mixed in the pore space and the associated partial saturation model is an ongoing research topic. In this context, it is worth clarifying the terminology conventionally used to describe the partial saturation models:

- Gassmann's equations (Gassmann, 1951) are commonly used even though they are defined for a single fluid saturating the pores. This requires deriving properties of an effective fluid phase to be plugged into the Gassmann's equations (Domenico, 1976). The widely used "Gassmann-Hill" or "Gassmann-Wood" wordings describe the way the effective fluid bulk modulus is calculated (Hill or Wood averages) and plugged into the Gassmann's equations for a single fluid phase.
- Lower and upper bounds for the effective fluid bulk modulus are defined by Reuss and Voigt averages, respectively (Mavko et al., 2009). The upper bound shows an almost linear dependency of P-wave velocity versus brine saturation while the lower bound shows a sharp P-wave velocity decrease as soon as a few percent of gas or supercritical CO_2 is present (fizz-gas effect). Curves describing these phenomena are given in e.g. Dupuy et al. (2017) and Papageorgiou et al. (2018).
- Depending on the way the fluid phases are mixed in the pore space, a full range of effective models falls between the lower and upper bounds. Brie et al. (1995) equation (given in Appendix A) is a convenient way to span the full range of models between these bounds by varying the exponent e called Brie, fluid mixing or patchiness exponent. Papageorgiou et al. (2016) propose a similar derivation for the patchiness exponent.
- "Patchy" and "uniform" saturations are terms often used to try to give a physical meaning to the way the effective fluid phase is calculated. Usually, "patchy saturation" corresponds to low fluid mixing exponent values (down to 1) and to curves close to the upper bound while "uniform saturation" corresponds to high fluid mixing exponent values (up to 40) and curves close to the lower bound. Depending on authors (Carcione et al., 2006; Queißer and Singh, 2013; Bergmann and Chadwick, 2015; Ghosh et al., 2015; Falcon--Suarez et al., 2018; Williams and Chadwick, 2012), the "patchy saturation" term is used for fluid mixing exponent values in the range from 1 to 5. As "patchy saturation" is not appropriate for an effective fluid phase (see next bullet point), we recommend using the term "patchy mixing" for behaviours close to the upper bound (fluid mixing exponent close to 1), and "uniform mixing" for behaviours close to the lower bound (fluid mixing exponent close to 40, with the two fluid phases being mixed at the finest scale) and "semi-patchy mixing" for all behaviours in between.
- The term "patchy saturation" refers to more complex rock physics theories based on the precursory works of White (1975) and Dutta and Odé (1979), where spherical patches of porous medium saturated with the more mobile fluid (supercritical CO_2) are embedded in the porous medium saturated with the least mobile fluid (brine). These models agree better with observed attenuations at seismic frequencies (Pride et al., 2004; Rubino et al., 2011). They are however difficult to use for quantitative inversion due to the large number of parameters involved in the models.

Laboratory measurements on Utsira sandstones (Falcon-Suarez et al., 2018) confirm that it is not straightforward to describe the way the brine and CO_2 phases are mixed together. Dupuy et al. (2017) also show that the introduction of the fluid mixing exponent as an additional degree of freedom causes a strong trade-off effect (between CO_2 saturation and the mixing exponent) which is difficult to resolve when P-wave velocity is the only input to the rock physics inversion.

5. Pore pressure effects and pressure-saturation discrimination

At Sleipner, where CO_2 is injected into a large open aquifer, the pressure build-up due to the injection is very weak and the pore pressure effects on geophysical observables are consequently negligible (Chadwick et al., 2012). These effects should, however, be considered for other CO_2 storage sites (e.g. Snøhvit (Grude et al., 2014), In Salah or Weyburn (Verdon et al., 2013)) because they can strongly affect the observed 4D effects on geophysical data (Landrø, 2001). Pore pressure is also a key parameter in addition to saturation to establish conformance analysis. We give here more details about the main geophysical observables (and related rock physics parameters) and their dependencies on the two main quantities we are interested in, i.e. CO_2 saturation (S_{CO_2}) and pore pressure (P_p). The main quantitative observables (with dependencies on pore pressure and CO_2 saturation highlighted with blue text) obtained from geophysical data are:

- the bulk density ρ (density model from seismic tomography or FWI or density changes from seabed gravimetric survey). It can be defined with respect to porosity φ and grain mineral and fluid densities, respectively ρ_s and ρ_f (the latter one being dependent on pore pressure and saturation):

$$\rho\left(S_{CO_2}, P_p\right) = (1-\phi)\rho_s + \phi\rho_f\left(S_{CO_2}, P_p\right) \tag{4}$$

- the resistivity R_t (from CSEM or ERT surveys), defined by Archie's law (Archie, 1942) with respect to brine resistivity R_w, porosity φ, and cementation m and saturation n exponents:

$$R_t\left(S_{CO_2}\right) = \frac{R_w}{\phi^m\left(1-S_{CO_2}\right)^n} \tag{5}$$

- the P-wave velocity V_P from seismic inversion (tomography, FWI, AVO inversion, velocity analysis, etc) defined with respect to saturated (undrained) porous medium bulk K_U and shear G moduli and bulk density ρ:

$$V_P\left(S_{CO_2}, P_p\right) = \sqrt{\frac{K_U\left(S_{CO_2}, P_p\right) + \frac{4}{3}G\left(P_p\right)}{\rho\left(S_{CO_2}, P_p\right)}} \tag{6}$$

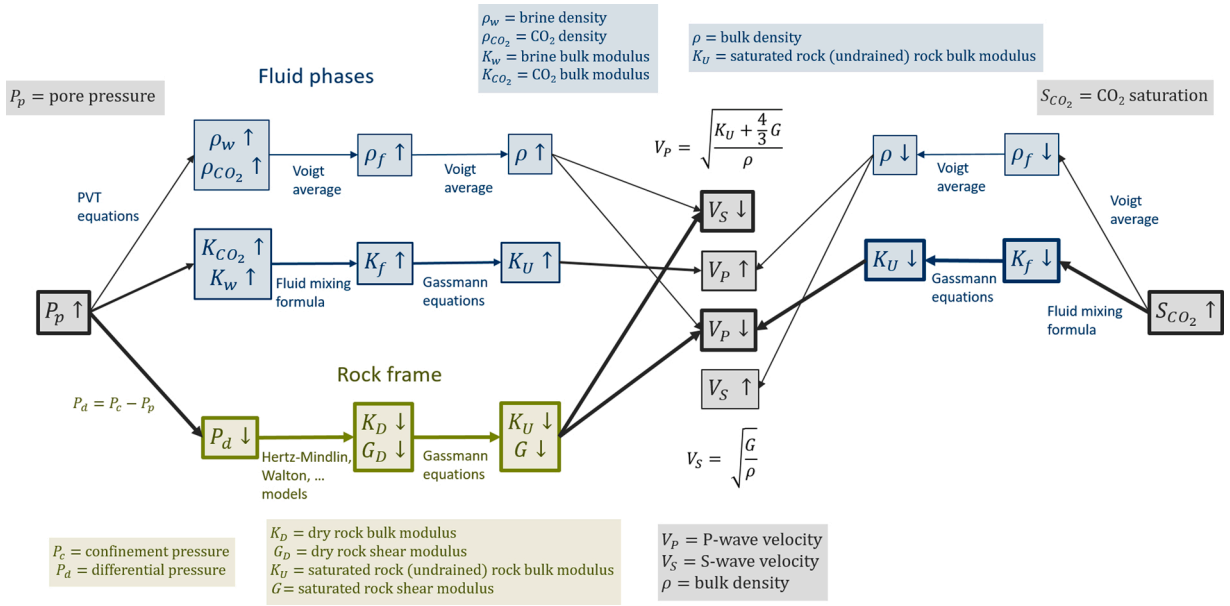

Fig. 2. Sketch summarizing the different dependencies between seismic observables and pore pressure and saturation changes. Due to CO_2 injection, pore pressure (P_p) and CO_2 saturation (S_{CO_2}) will increase. Pore pressure will both affect the fluid phase properties (top left) and the rock frame properties (bottom left), leading to effects on seismic observables, e.g. decrease of P-wave velocity. On the other hand, the change of saturation will affect fluid bulk modulus and density, leading to a change in seismic observables as well, e.g. a decrease in P-wave velocity. The thicker arrows and boxes are the dominating effects. The detailed equations and dependencies are given in the text.

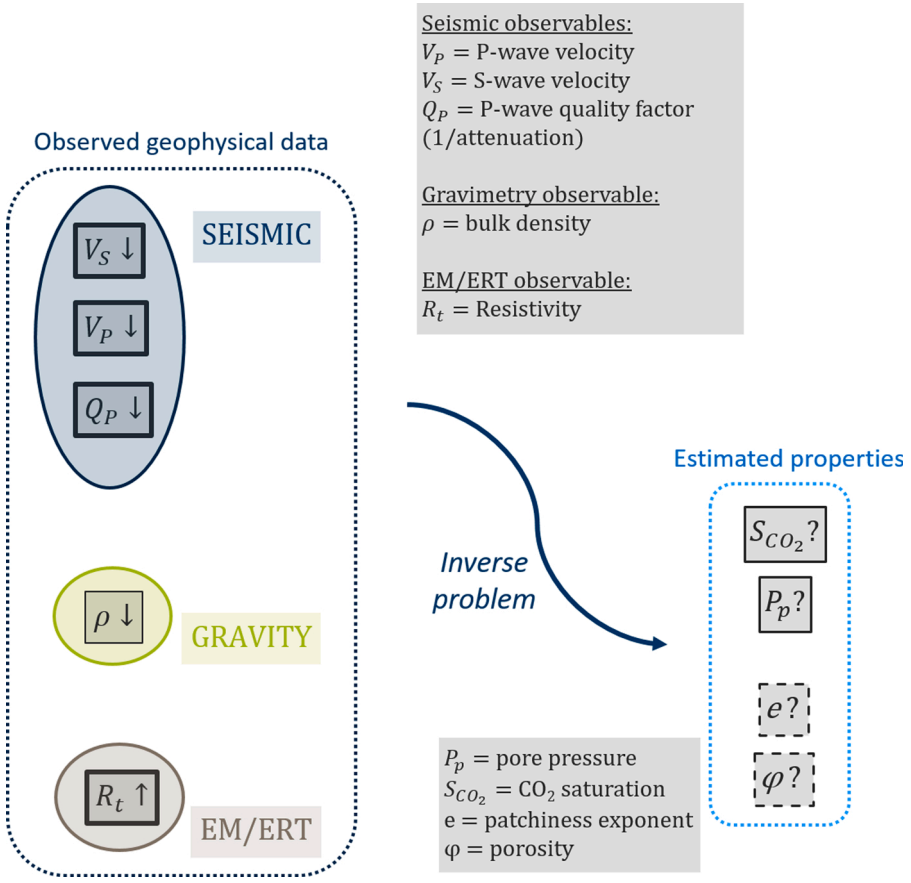

Fig. 3. Sketch summarizing the inverse problem when CO_2 injection is affecting geophysical observables and the link with pore pressure and saturation changes (and fluid mixing exponent and porosity).

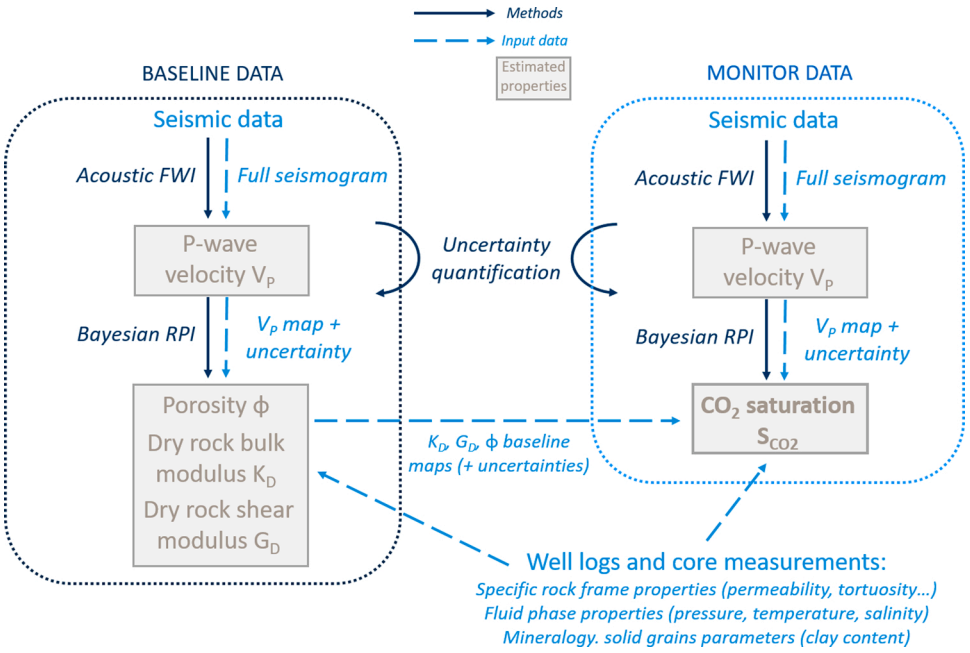

Fig. 4. Schematic framework of the quantitative monitoring at Sleipner including uncertainty assessment and time-lapse strategy. FWI stands for Full Waveform Inversion and RPI stands for Rock Physics Inversion. The two-step workflow described in Fig. 1 is used for baseline (left) and monitor (right) stages. The details of each method (acoustic FWI, uncertainty quantification for FWI, Bayesian RPI) are given in the text. The rock physics parameters derived in the first stage (K_D, G_D and ϕ) as well as the data from well logs and core measurements are used as prior models in the rock physics inversion.

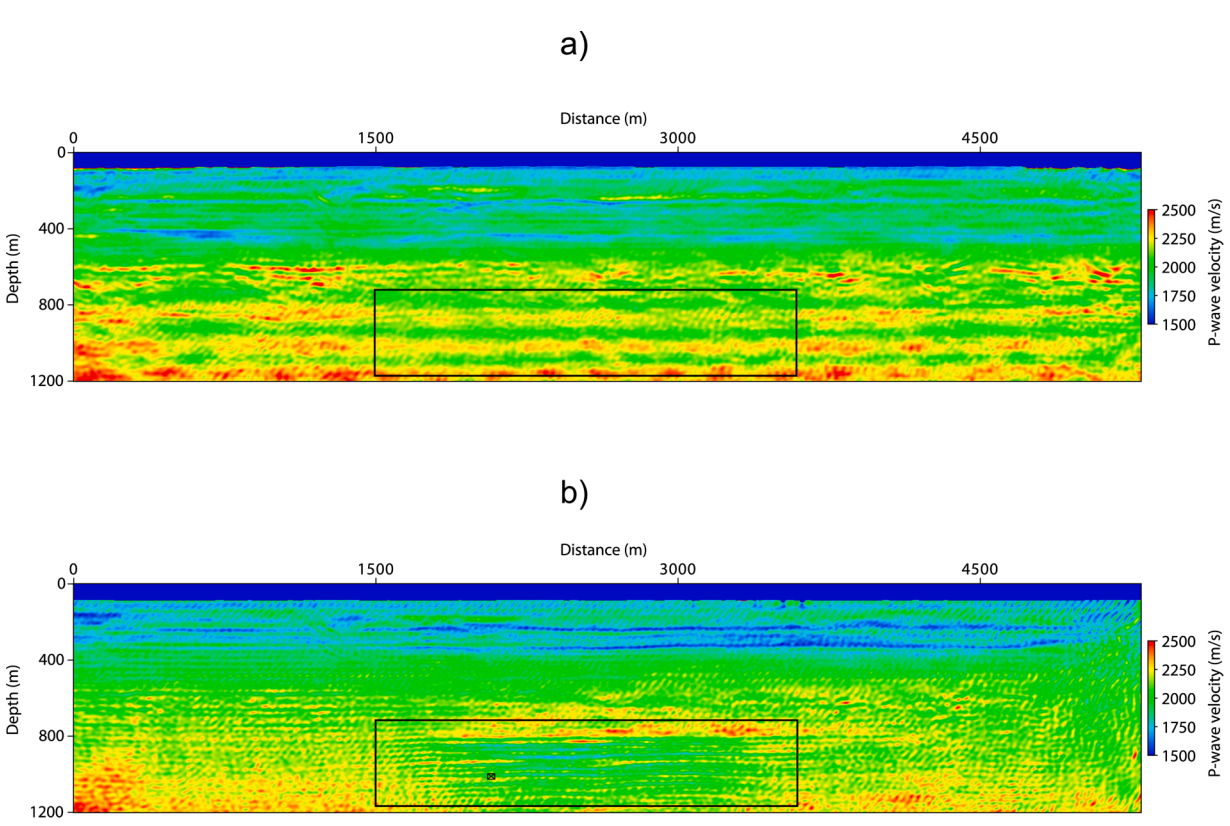

Fig. 5. P-wave velocity models obtained by acoustic FWI for baseline (a) and monitor (b) vintages. Input seismic data are extracted from the 3D seismic survey at Sleipner (inline number 1874). The rectangles give the location of the target model area used for the rock physics inversion tests (displayed in Fig. 6). The small cross rectangle stands for the projection of the injection point.

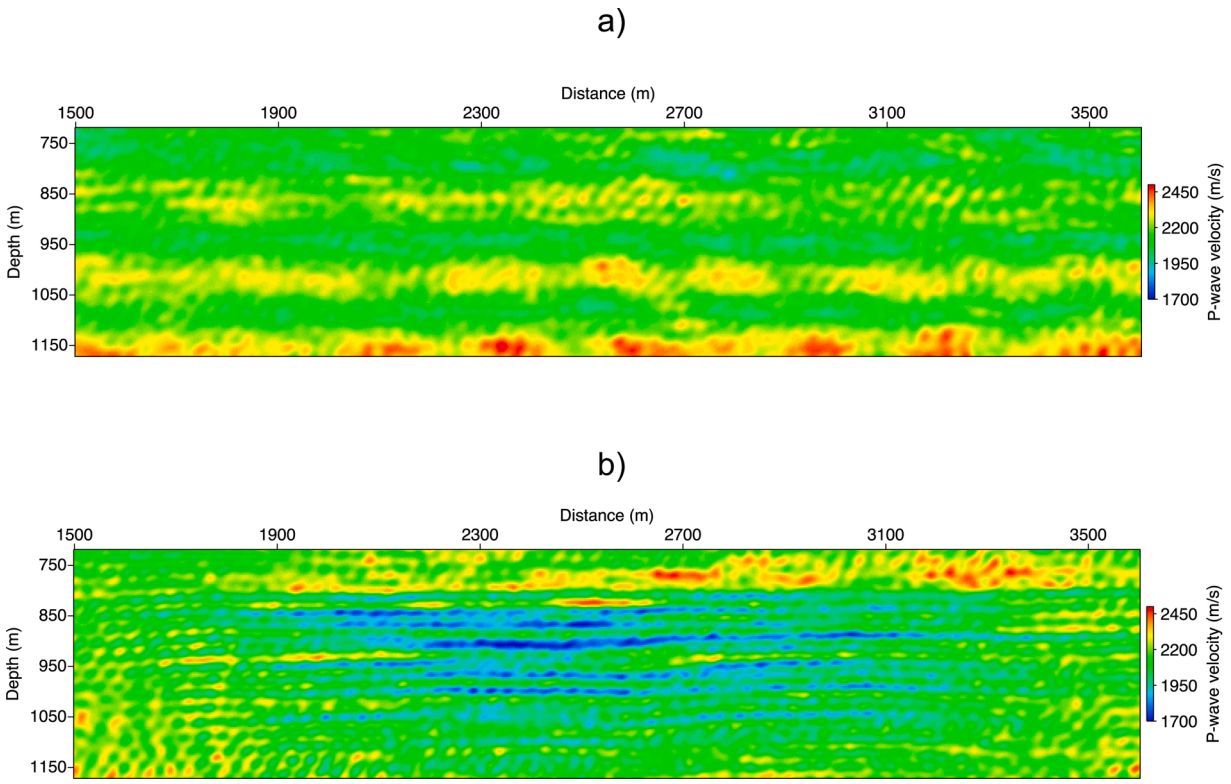

Fig. 6. Close ups of the corresponding P-wave velocity models target areas obtained by acoustic FWI for (a) baseline and (b) monitor vintages. These close-ups are extracted from the models given in Fig. 5.

- the S-wave velocity V_S from seismic inversion (elastic FWI, AVO inversion, velocity analysis, surface wave tomography, etc) defined with respect to saturated (undrained) porous medium shear modulus G and bulk density ρ:

$$V_S(S_{CO_2}, P_p) = \sqrt{\frac{G(P_p)}{\rho(S_{CO_2}, P_p)}} \tag{7}$$

- the quality factors (seismic attenuations) can also give information about P_p and S_{CO_2} but are more difficult to estimate.

The detailed formulas, including Gassmann's (Gassmann, 1951) and effective fluid phase equations are given in Appendix A. Fig. 2 summarizes the effects of pore pressure and saturation changes on the seismic observables. It is worth noting that the sensitivities of geophysical properties to pore pressure and saturation changes are quite different, i.e.:

- the saturation S_{CO_2} is affecting the resistivity R_t and the bulk density ρ via the effective fluid density ρ_f. It is affecting seismic velocities V_P and V_S via bulk density ρ and porous medium bulk modulus K_U (only V_P).
- the pore pressure P_p is affecting bulk density ρ via the effective fluid density ρ_f and the seismic velocities via the bulk density ρ and the porous medium bulk modulus K_U. Looking more in details (see full formulation in Appendix A), the effect of the pore pressure can be divided into two parts:
  - on one hand, the effective fluid properties (density ρ_f and bulk modulus K_f) are dependent on pore pressure. Pressure-Volume-Temperature (PVT) thermodynamics models (Span and Wagner, 1996; Lindeberg, 2013) or more empirical models (Batzle and Wang, 1992) can be used to derive pore pressure (but also temperature and salinity) dependencies of each fluid phases. The effective fluid phase is then calculated via various averages (Reuss, Voigt, Brie averages) given in Appendix A.
  - on the other hand, the dry rock frame bulk K_D and shear G_D moduli involved in the Gassmann's equations are the only parameters dependent on pore pressure. Basically, when pore pressure increases, the rock frame (arrangement of grains) is modified, and its mechanical moduli decrease. Many models (empirical, phenomenological or based on physical principles) exist to link rock frame moduli to differential pressure (equal to confinement pressure minus pore pressure). Screening the validity and complexity of these models is out of the scope of this paper, but the reader is referred to Hertz-Mindlin (Mindlin, 1949; Mavko et al., 2009), Walton (Walton, 1987; Pride, 2005), pore space stiffness (Mavko and Mukerji, 1995; Dinh and Van der Baan, 2019), compliant porosity (Shapiro, 2003; Shapiro and Kaselow, 2005), or cracks (Sayers and Kachanov, 1995; Pride et al., 2017) models for more details on the different approaches.

Deriving pressure effects from geophysical observables (especially seismic data) is not straightforward as pressure effects are competitive with saturation effects. Fig. 3 summarizes the complexity of the inverse problem when different rock properties are affected by the CO_2 injection and these changes have variable effects on the geophysical observables. A simple approach based on AVO parameters changes (Landrø, 2001) can discriminate pressure and saturation in specific cases but more advanced approaches are required for quantitative estimations. Including the rock physics models with pressure-dependent rock physics properties (both fluid and rock frame parameters) in our rock physics inversion algorithms is straightforward. However, optimal model parametrization is complex and requires additional inputs. Joint rock physics inversion is then even more meaningful. We can also think that

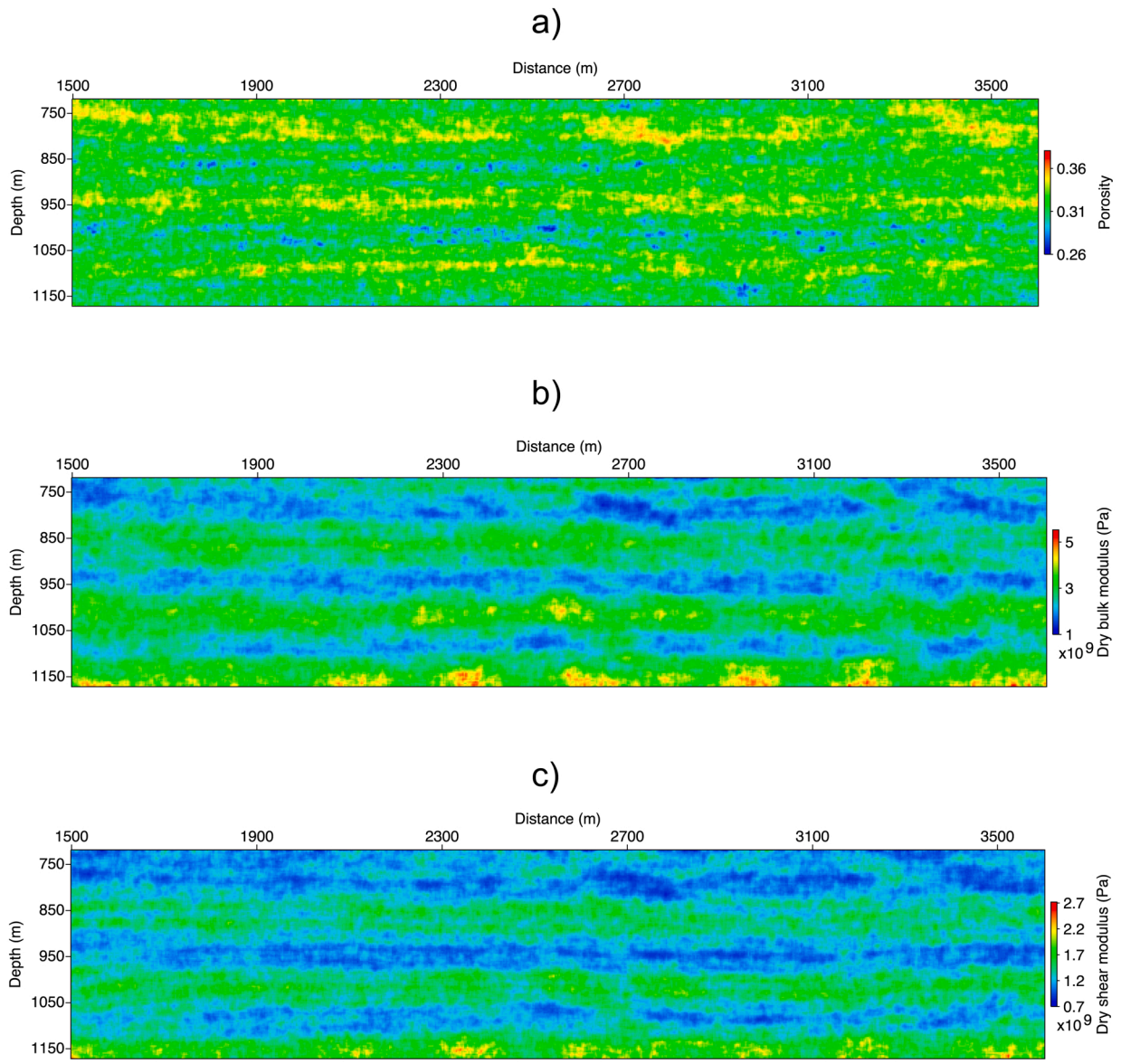

Fig. 7. Estimated reservoir properties: a) porosity, b) dry bulk and c) shear moduli before injection. The input data of this rock physics inversion is the P-wave velocity map obtained by FWI and given in Fig. 6a.

extracting more information from the seismic data, using multiparameter inversion will be valuable. For example, saturation can strongly affect the seismic attenuations (Pride et al., 2004; Rubino et al., 2011). On the other hand, seismic shear wave propagation is mainly affected by pressure effect (saturation playing only a minor role in the bulk density term), so combining P- and S-wave velocity data might be valuable to handle the trade-offs between saturation and pore pressure effects. As our real data application focuses on the Sleipner dataset, pore pressure effects are not considered in the following section.

6. Case study at Sleipner using baseline and monitor seismic data

We present an application of the two-step quantitative approach to Sleipner CO_2 storage monitoring data. The workflow is summarized in Fig. 4. We use prestack seismic data from 1994 (before CO_2 injection, baseline) and 2008 vintages (after 12 years of injection, around 10.15 Mt CO_2 injected, monitor). The two-step process is first applied to the baseline data for the estimation of selected reservoir properties, with uncertainty, prior to injection. Then, in a second stage, the same process is applied to the monitor data, where, in addition, the rock physics inversion is using information derived from the baseline results as prior knowledge. For both baseline and monitor inversions, prior models of mineral grains and fluids properties are defined from log and core measurements. The models for the monitor inversion are also partially derived from baseline inversion, especially the rock frame properties (porosity and dry bulk and shear moduli). Similar tests are run for the seismic inline 1836 (Yan et al., 2019). We present here the results for the inline 1874 which is located further away from the injection point and following the main channel path towards North (Furre et al., 2015).

We perform two separate acoustic FWI runs (baseline and monitor) using frequencies up to 33 Hz. Following the workflow presented in Fig. 4, we first obtain high-resolution 2D P-wave velocity models (Fig. 5) and we select a target area around the injection point where the CO_2 is expected to migrate (Fig. 6). Local uncertainty assessment is carried out providing a posterior covariance matrix. P-wave velocity models around the target are compared between baseline and monitor cases. The signature of the injected CO_2 is clearly visible through a velocity drop of

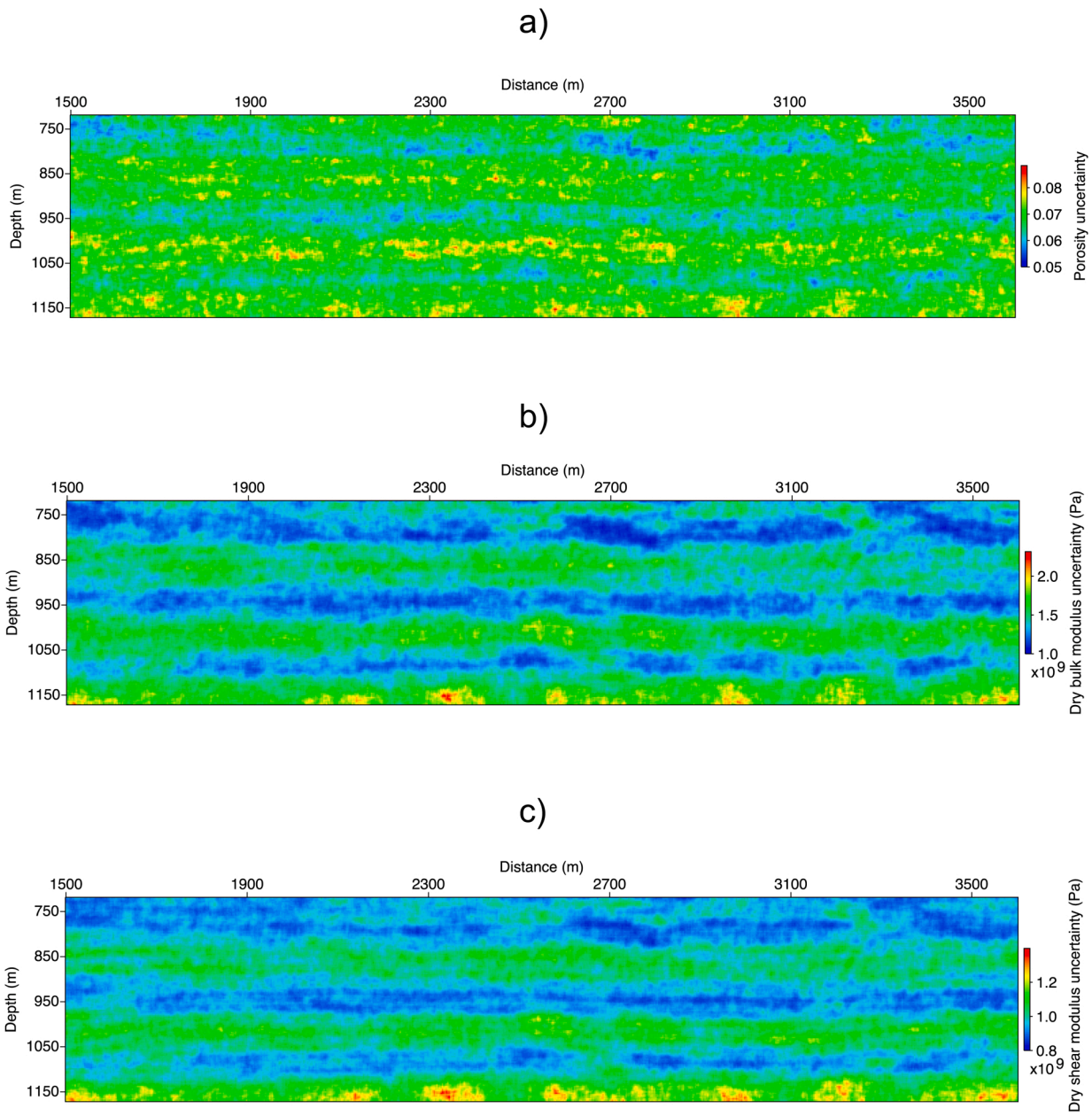

Fig. 8. Uncertainties in estimated reservoir properties: a) porosity, b) dry bulk and c) shear moduli before injection. These uncertainties are related to the estimates given in Fig. 7.

a few hundred m/s (Fig. 6). Velocities outside of the target area (overburden and underburden especially) are slightly different between the baseline and monitor inversions while there are supposed to not be affected by the CO_2 injection. This can be explained by several factors, among them being the difference in data quality between the two surveys (1994 versus 2008), some uncertainty propagation outside of the target due to smearing effects (Queißer and Singh, 2013; Romdhane and Querendez, 2014) and uncertainties due to the limited available offset range of the seismic data.

In the second stage, rock physics inversion is applied using the input P-wave velocity model derived from the first stage using baseline data. Prior to CO_2 injection, we focus on relevant reservoir parameters, namely porosity, bulk and shear rock frame moduli (Fig. 7). We use well logs and core measurements from the literature (Bøe and Zweigel, 2001; Chadwick et al., 2004; Ghaderi and Landrø, 2009; Falcon-Suarez et al., 2018) to define prior values of the other poroelastic parameters, i.e. fluid parameters (full saturation of brine whose properties are dependent on pressure and temperature), mineral grain parameters (the mineral compositions of Utsira sandstone reservoir and Nordland shale caprock are well-known) and additional rock frame properties (permeability and cementation factor). We notice a high porosity (low bulk and shear moduli) layer between 900 and 1000 m depth. Assuming multivariate Gaussian distributions, we derive uncertainties in porosity and dry rock moduli estimates (Fig. 8). The uncertainties in the three rock frame parameters are higher when the porosity is low and when the dry bulk and shear moduli are high, i.e. in less good reservoir quality layers.

Given that the Utsira sand is purely siliciclastic (no carbonate minerals) and that the pressure build-up is negligible (Chadwick et al., 2012), it is meaningful to assume that the porosity and dry rock moduli estimated with baseline data will not change due to CO_2 injection. We consequently use the porosity, bulk and shear dry rock moduli mapping as prior knowledge (fixed values) for the rock physics inversion of monitor data (second stage, see workflow in Fig. 4). Using the P-wave velocity model and associated uncertainty derived from monitor seismic

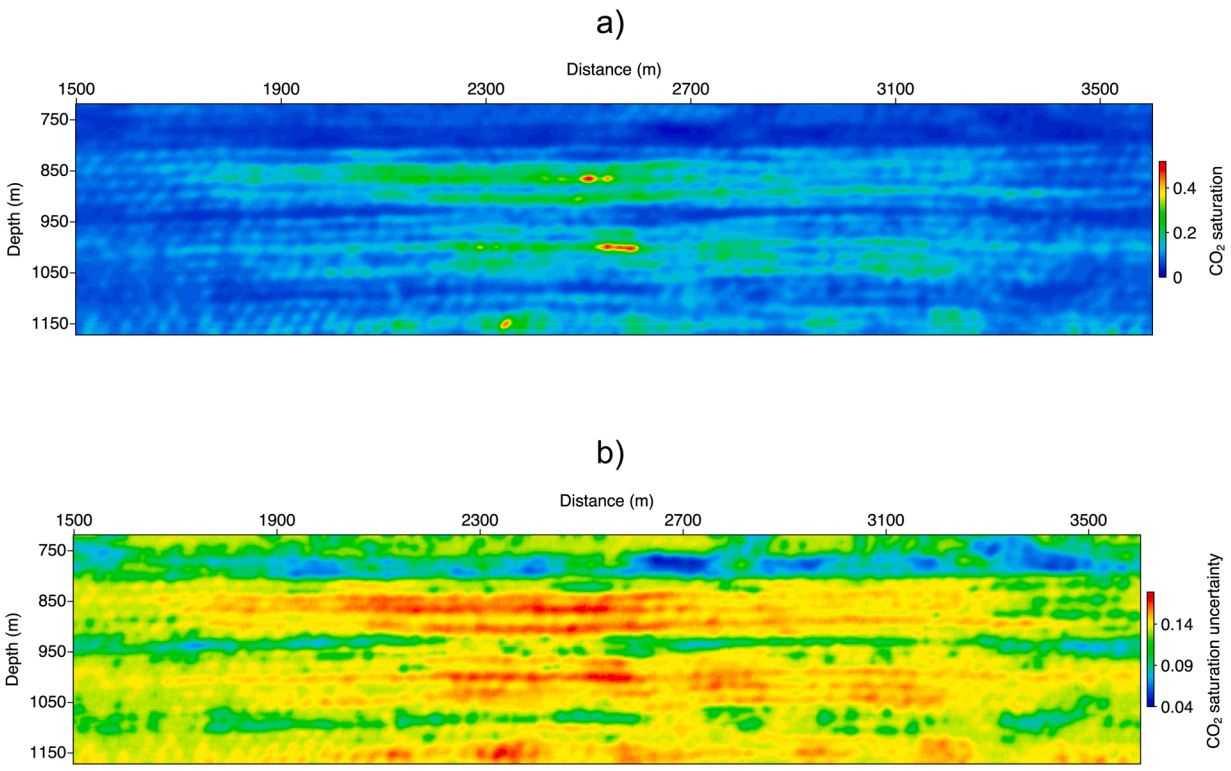

Fig. 9. Estimated CO_2 saturation (a) and associated uncertainties (b). The input data of this rock physics inversion is the P-wave velocity map obtained by FWI and given in Fig. 6b. Rock physics properties obtained in the baseline stage (Fig. 7) are also used as prior models.

data (Fig. 6b), and prior models from baseline rock physics inversion (Fig. 7) and well logs and core data, the spatial distribution of CO_2 saturation is estimated with uncertainty assessment (Fig. 9). High CO_2 saturations (up to 50 %) are observed in the top layers, between 850 and 900 m depth and between 950 and 1050 m depth. The caprock is located at 850 m depth approximately. The high saturation top layer is widely spread laterally while presence of CO_2 deeper down with saturation around 20 % is more localized. The uncertainties in saturation are slightly varying in space, between 10 and 20 % uncertainty in absolute values. It is worth noting that the very low CO_2 saturation values above the primary seal at 800 m depth are consistent with zero saturation values (given the associated, equally low, uncertainty). This confirms containment of the CO_2 in the main reservoir.

The CO_2 estimates presented in Fig. 9 are obtained with a fixed value of fluid mixing exponent: $e = 5$. Fig. 10 shows joint estimation of CO_2 saturation and fluid mixing exponent with the same input data. CO_2 saturation distribution and amplitudes are similar to those of Fig. 9, with a higher saturation uncertainty when the fluid mixing exponent is inverted for due to the higher number of degrees of freedom in the inverse problem. The results also show that the fluid mixing exponent is higher (suggesting more "uniform mixing") for high CO_2 saturations. The uncertainties in the fluid mixing exponent are quite constant where the CO_2 is present, i.e. between 5 and 10 in absolute values.

To constrain the trade-off between these two parameters (saturation and fluid mixing exponent), Subagjo et al. (2018) propose to combine the input from seismic and electromagnetic inversions in a joint rock physics inversion process. The synthetic test results of Fig. 11 and Table 1 illustrate how combining resistivity and P-wave velocity inputs result in reduced uncertainty on saturation estimates. Synthetic "one point" inversions are run based on generic Utsira sand properties. The results of Fig. 11 show the distribution of low misfit models and the trade-off between saturation and fluid mixing exponent. When the P-wave velocity is considered, we observe that values between 0 and 75 % of CO_2 saturation associated with values between 1 and 40 of fluid mixing exponent fit the input data well. This trade-off is also observed when P-and S-wave velocities or P-wave velocity and bulk density inputs are considered. However, when P-wave velocity is combined with bulk resistivity, these "low misfit" models are localised in the vicinity of the true model with a smaller spread.

Table 1 gives more insights about this trade-off between saturation and fluid mixing exponent and how to solve it by integrating more input data. When only P-wave velocity is used as input, the inversion system is highly underdetermined (one input data, two free parameters to be inverted, the other rock physics parameters being fixed in this test) and the obtained values (lowest misfit model) are far from the true model (5–25% of error). As soon as an additional input data is considered in addition to P-wave velocity (S-wave velocity, bulk density or bulk resistivity), the inversion is converging towards the true model and the errors of estimations are quite low (0.03–1.23% of error depending on the case and the parameter). However, as observed in Fig. 11, the spread of the misfit/likelihood function is quite large for the cases where V_P is combined with V_S or ρ. This is leading to large uncertainties in the estimation of the CO_2 saturation and fluid mixing exponent even if the inversion is converging towards the true model. When the P-wave velocity is combined with the bulk resistivity, the estimation error is very low for both parameters (0.005 and 0.41 % for S_{CO_2} and e respectively) and the uncertainty in these estimates is also quite small as shown in Fig. 11d.

To summarize, the trade-off between saturation and fluid mixing exponent is only slightly reduced when additional seismic or gravity data is used (shear wave velocity and density) while the use of resistivity in combination with P-wave velocity is critical to ensure good convergence and low uncertainty for saturation and fluid mixing exponent. This observation is valid for the Sleipner data but the trends might be different for other cases where the pore pressure effect is not negligible, i.e. where the injection affects the rock frame properties in addition to the fluid properties.

From a practical point of view, deriving resistivity maps is done using

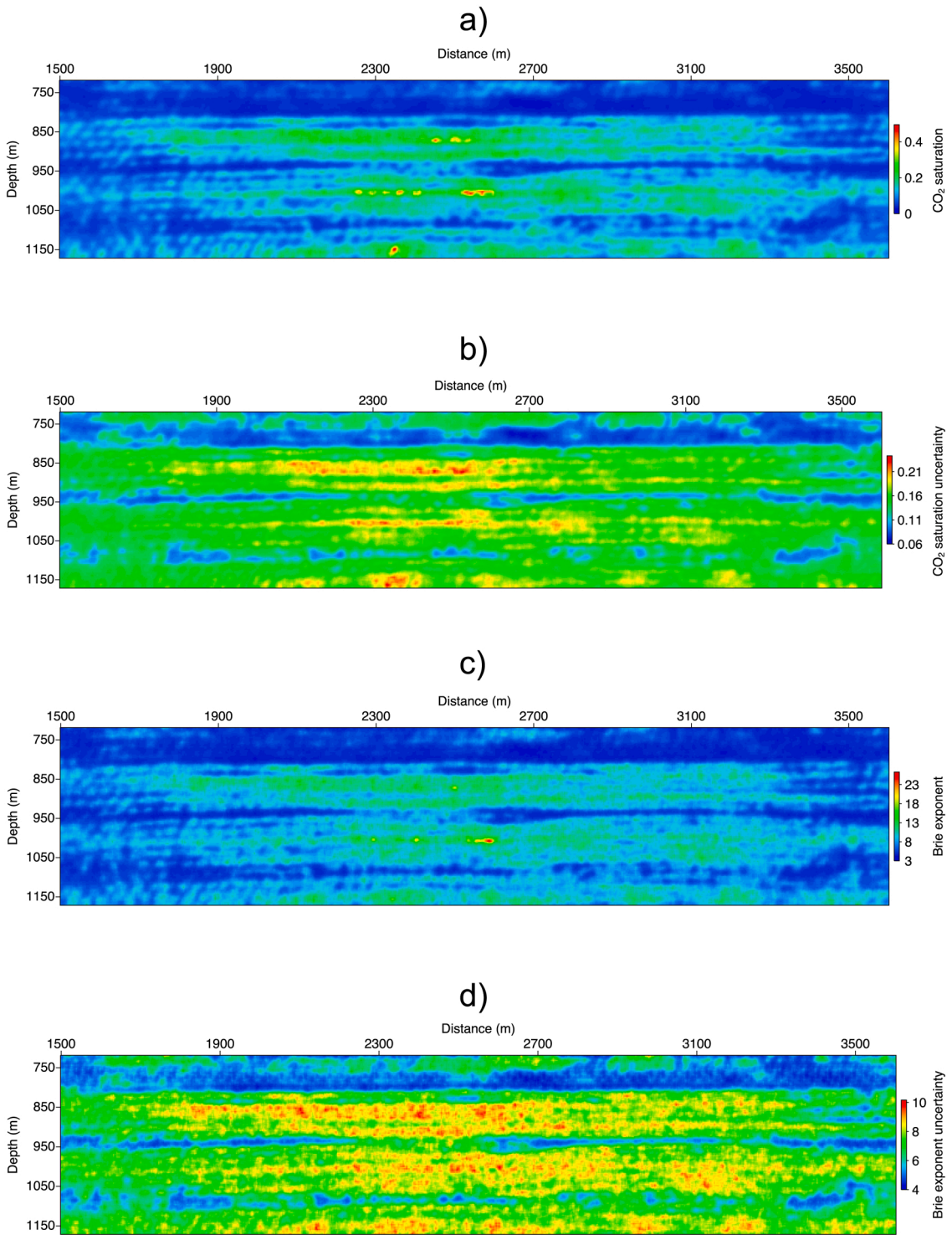

Fig. 10. Estimated CO_2 saturation and associated uncertainties in case of joint inversion of saturation and fluid mixing exponent. The fluid mixing exponent (Brie exponent) and associated uncertainties are also given. a) CO_2 saturation, b) uncertainty in CO_2 saturation, c) fluid mixing exponent and d) uncertainty in fluid mixing exponent. The input data of this rock physics inversion is the P-wave velocity map obtained by FWI and given in Fig. 6b. Rock physics properties obtained in the baseline stage (Fig. 7) are also used as prior models.

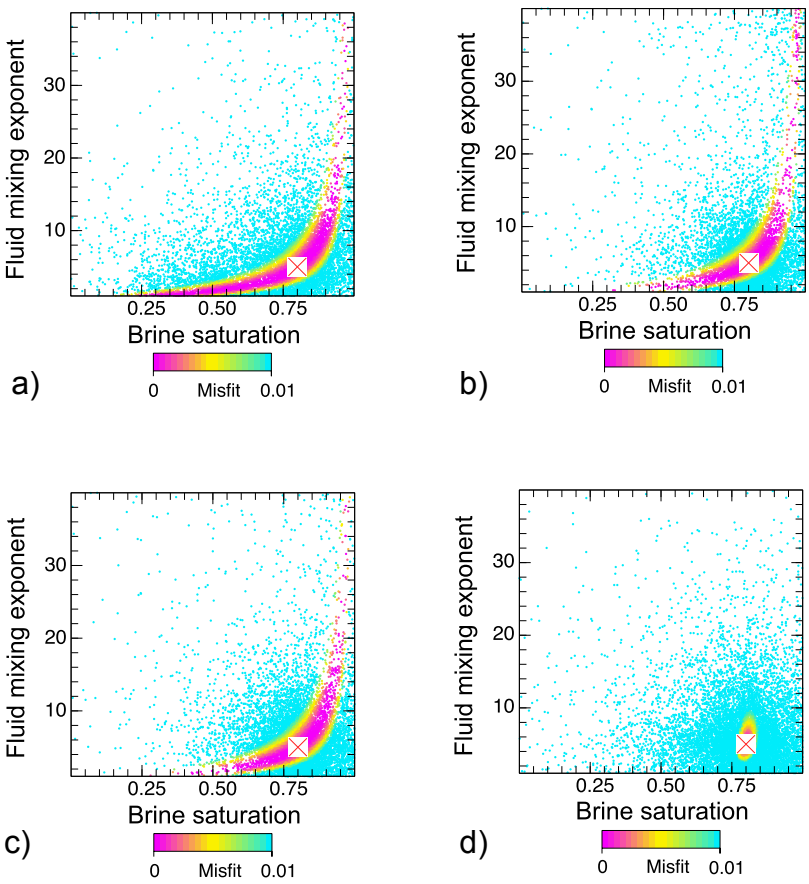

Fig. 11. Inversion results from synthetic data tests for estimation of CO_2 saturation (1 – brine saturation) and fluid mixing exponent ($e = 1$ being patchy mixing and $e = 40$ being uniform mixing) at a single point in space. Four different input data parametrizations are represented: a) V_P, b) $V_P + V_S$, c) $V_P + \rho$ and d) $V_P + R_t$ (V_P and V_S are P- and S-wave velocities, ρ is the bulk density and R_t is the bulk resistivity). The red cross is the true model ($S_{CO_2} = 20$ %, $e = 5$ = semi-patchy mixing). Each point is an inversion model with a colour associated with a misfit between 0 and 1%. The models with the lowest misfit found are given in Table 1. The results of Figure a), in which V_P is the only input data, correspond to results for a single point of Fig. 10 and are modified after Yan et al. (2019).

Table 1
Best estimated models of CO_2 saturation (1-S_w) and fluid mixing exponent e showing the lowest misfit in the tests shown in Fig. 9. The true values are $S_{CO_2} = 20$ % ($S_w = 80$ %) and $e = 5$. The results are given for various combinations of P-wave velocity V_P, S-wave velocity V_S, bulk density ρ and bulk resistivity R_t.

Input data	Parameter	Best model	Deviation from true value (%)
V_P	S_w (%)	83.7	4.63
	e	6.25	25
$V_P + V_S$	S_w (%)	80.2	0.25
	e	5.06	1.2
$V_P + \rho$	S_w (%)	80.02	0.025
	e	5.02	0.4
$V_P + V_S + \rho$	S_w (%)	79.99	0.0125
	e	5.002	0.04
$V_P + R_t$	S_w (%)	80.004	0.005
	e	5.02	0.4

CSEM in offshore settings (Bhuyian et al., 2012; Park et al., 2013) or ERT surveys (Bergmann et al., 2012; Commer et al., 2016) (mainly onshore, with well-to-surface and cross-well acquisitions). The resolution is nevertheless not comparable to seismic inversion results and scaling issues must be addressed carefully. Different joint inversion approaches (Dell'Aversana, 2014; Colombo and Rovetta, 2018; Giraud et al., 2019) can be used but are not within the scope of this paper. At Sleipner, only one 2D CSEM survey has been acquired in 2008 with a different survey azimuth compared to the one used for the 3D seismic survey acquired in the same year. To run joint inversion on the Sleipner datasets, it is thus needed to work with the 3D seismic data or to consider 1D profiles where the CSEM and seismic inlines are crossing.

7. Conclusions

We describe a quantitative monitoring approach which relies on a two-step inversion methodology. The first step consists of conventional geophysical inversion while the second step, the rock physics inversion, uses the results of the first step as input. Uncertainty is assessed in both stages and accounted for via a Bayesian formulation. Quantitative estimates of relevant rock physics properties such as porosity, rock frame moduli, CO_2 saturation, fluid mixing/distribution are then derived from geophysical data.

We show an example of inversion of Sleipner data where seismic FWI is combined with rock physics inversion to estimate (1) rock frame properties (using baseline data, before CO_2 injection) and (2) CO_2 saturation and fluid mixing exponent using monitor data. We estimate CO_2 saturation values between 0 and 50 % showing a migration towards high porosity upper layers. When the fluid mixing exponent is inverted together with the saturation, similar saturation distributions are obtained but with higher uncertainty. Estimates of CO_2 saturation above the seal are close to 0 % with low uncertainty, confirming containment within the main reservoir.

We show that it is recommended to combine seismic P-wave velocity with resistivity inputs to mitigate the trade-off between the saturation and the fluid mixing exponent and reduce the uncertainty in their estimates. We also show that discriminating pressure and saturation effects from geophysical observables is not straightforward and can benefit from a multi-physics-based approach.

The proposed approach is useful for conformance verification, i.e. ensuring that observed time-lapse effects due to CO_2 injection are consistent with a fluid flow-based modelling prognosis. CO_2 saturations derived from inversion may be compared to predicted saturations from reservoir modelling (Watson et al., 2019). This in turn can support

history matching processes where the update of fluid flow-based reservoir models is addressed by Ensemble Kalman Filter (EnKF) methods (Evensen, 2009) or by building an optimisation problem where the reservoir model is updated by monitoring results (Vasco et al., 2019; Anyosa et al., 2019).

Declaration of Competing Interest

The authors report no declarations of interest.

Acknowledgments

This publication has been produced with support from the NCCS Centre, performed under the Norwegian research program Centres for Environment-friendly Energy Research (FME). The authors acknowledge the following partners for their contributions: Aker Solutions, Ansaldo Energia, Baker Hugues, CoorsTek Membrane Sciences, EMGS, Equinor, Gassco, Krohne, Larvik Shipping, Lundin, Norcem, Norwegian Oil and Gas, Quad Geometrics, Total, Vår Energi, and the Research Council of Norway (257579/E20). The Bayesian Rock Physics Inversion tool used is developed in the SINTEF-coordinated Pre-ACT project (Project No. 271496) funded by Total, Equinor, Shell, TAQA, RCN (Norway), Gassnova (Norway), BEIS (UK), RVO (Netherlands), and BMWi (Germany) and co-funded by the European Commission under the Horizon 2020 programme, ACT Grant Agreement No 691712. Malcolm Sambridge is also acknowledged for providing Neighbourhood Algorithm used to solve the rock physics inversion problem. We also thank Joonsang Park (NGI) for fruitful discussions regarding Sleipner CSEM dataset. We acknowledge two anonymous reviewers for their useful comments that have greatly improved the manuscript.

Appendix A

Gassmann's equations and effective fluid relationships

The Gassmann's equations (Gassmann, 1951) allows calculating the saturated (undrained) bulk K_U and shear G moduli of the single fluid saturated porous medium from the dry rock frame bulk K_D and shear G_D moduli, the porosity φ, the mineral grains bulk modulus K_s and the fluid phase bulk modulus K_f. The Gassmann's equations are given here with underlined dependencies to pore pressure P_p and CO_2 saturation S_{CO_2}:

$$K_U\left(S_{CO_2}, P_p\right) = \frac{\phi K_D\left(P_p\right) + \left(1 - (1+\phi)\frac{K_D\left(P_p\right)}{K_s}\right) K_f\left(S_{CO_2}, P_p\right)}{\phi\left(1 + \Delta\left(S_{CO_2}, P_p\right)\right)} \tag{8}$$

$$G\left(P_p\right) = G_D\left(P_p\right) \tag{9}$$

With the additional Δ parameter defined as:

$$\Delta\left(S_{CO_2}, P_p\right) = \frac{1-\phi}{\phi}\frac{K_f\left(S_{CO_2}, P_p\right)}{K_s}\left(1 - \frac{K_D\left(P_p\right)}{(1-\phi)K_s}\right) \tag{10}$$

As mentioned in the main text, the Gassmann's equations are derived for a porous medium saturated with a single fluid. Effective fluid properties must be calculated to be plugged into these equations. The effective fluid density is usually calculated with an arithmetic average such as:

$$\rho_f\left(S_{CO_2}, P_p\right) = \left(1 - S_{CO_2}\right)\rho_w\left(P_p\right) + S_{CO_2}\rho_{CO_2}\left(P_p\right) \tag{11}$$

Brine and CO_2 densities are dependent on pore pressure (and the brine density is also dependent on temperature and salinity) and can be estimated with empirical relationships (Batzle and Wang, 1992) or complex models based on thermodynamics (Span and Wagner, 1996, Lindeberg, 2013). There are several ways to calculate the effective fluid bulk modulus (discussed in detail in the main text). The Brie relation (Brie et al., 1995) is given (with respect to the fluid mixing or fluid mixing exponent e) by:

$$K_f\left(S_{CO_2}, P_p\right) = \left(K_w\left(P_p\right) - K_{CO_2}\left(P_p\right)\right)\left(1 - S_{CO_2}\right)^e + K_{CO_2}\left(P_p\right) \tag{12}$$

Similar to densities, the brine and CO_2 bulk moduli are dependent on pore pressure and can be calculated with empirical or thermodynamic-based models. Alternative ways to calculate the effective fluid bulk modulus are the Reuss average (lower bound), corresponding to high numbers of fluid mixing exponents (up to 40) and so-called "uniform mixing":

$$\frac{1}{K_f\left(S_{CO_2}, P_p\right)} = \frac{\left(1 - S_{CO_2}\right)}{K_w\left(P_p\right)} + \frac{S_{CO_2}}{K_{CO_2}\left(P_p\right)} \tag{13}$$

or the Voigt average (upper bound), corresponding to low numbers of fluid mixing exponents (down to 1) and so-called "patchy mixing":

$$K_f\left(S_{CO_2}, P_p\right) = \left(1 - S_{CO_2}\right) K_w\left(P_p\right) + S_{CO_2}K_{CO_2}\left(P_p\right) \tag{14}$$

Papageorgiou et al. (2016) and Wollner and Dvorkin (2018) give Brie-like relationships and different expressions of the fluid mixing exponent.

References

Anyosa, S., Bunting, S., Eidsvik, J., Romdhane, A., 2019. A Simulation Analysis of CO_2 Capture and Underground Storage Monitoring in Smeaheia. EAGE Petroleum Geostatistics, Florence, Italy.

Archie, G.E., 1942. The electrical resistivity log as an aid in determining some reservoir characteristics. Trans. Am. Inst. Mining Metall. Eng. 146, 55–62.

Arts, R., Eiken, O., Chadwick, A., Zweigel, P., van der Meer, L., Zinszner, B., 2004. Monitoring of CO_2 injected at sleipner using time-lapse seismic data. *Energy*, 29: 1383–1392. 6th International Conference on Greenhouse Gas Control Technologies.

Ayani, M., Grana, D., Liu, M., 2020. Stochastic inversion method of time-lapse controlled source electromagnetic data for CO_2 plume monitoring. Int. J. Greenhouse Gas Control 100, 103098.

Azevedo, L., Demyanov, V., 2019. Multiscale uncertainty assessment in geostatistical seismic inversion. Geophysics 84 (3), R355–R369.

Azevedo, L., Grana, D., Amaro, C., 2019. Geostatistical rock physics AVA inversion. Geophys. J. Int. 216 (3), 1728–1739.

Batzle, M., Wang, Z., 1992. Seismic properties of pore fluids. Geophysics 57 (11), 1396–1408.

Bergmann, P., Chadwick, A., 2015. Volume bounds on subsurface fluid substitution using 4D seismic time shifts with an application at Sleipner, North Sea. Geophysics 80 (5), B153–B165.
Bergmann, P., Schmidt-Hattenberger, C., Kiessling, D., Rücker, C., Labitzke, T., Henninges, J., Baumann, G., Schütt, H., 2012. Surface-downhole electrical resistivity tomography applied to monitoring of CO_2 storage at Ketzin, Germany. Geophysics 77 (6), B253–B267.
Bhuyian, A.H., Landrø, M., Johansen, S.E., 2012. 3D CSEM modeling and time-lapse sensitivity analysis for subsurface CO2 storage. Geophysics 77 (5), E343–E355.
Biot, M., 1962. Mechanics of deformation and acoustic propagation in porous media. J. Appl. Phys. 1482–1498.
Bøe, R., Zweigel, P., 2001. Characterisation of the Nordland Shale in the Sleipner Area by XRD Analysis - A Contribution to the Saline Aquifer CO_2 Storage (SACS) Project. SINTEF report (33.0764.00/01/01):1–23.
Bosch, M., Mukerji, T., Gonzalez, E.F., 2010. Seismic inversion for reservoir properties combining statistical rock physics and geostatistics: a review. Geophysics 75 (5), 75A165–75A176.
Bourne, S., Crouch, S., Smith, M., 2014. A risk-based framework for measurement, monitoring and verification of the Quest CCS Project, Alberta, Canada. Int. J. Greenh. Gas Control. 26, 109–126.
Brie, A., Pampuri, F., Marsala, A., Meazza, O., 1995. Shear sonic interpretation in gas-bearing sands. In: SPE Annual Technical Conf., 30595, pp. 701–710.
Bui-Thanh, T., Ghattas, O., Martin, J., Stadler, G., 2013. A computational framework for infinite-dimensional bayesian inverse problems part i: the linearized case, with application to global seismic inversion. SIAM J. Sci. Comput. 35 (6), A2494–A2523.
Buland, A., Omre, H., 2003. Bayesian linearized AVO inversion. Geophysics 68 (1), 185–198.
Carcione, J., Picotti, S., Gei, D., Rossi, G., 2006. Physics and seismic modeling for monitoring CO_2 storage. Pure Appl. Geophys. 163, 175–207.
Chadwick, R., Noy, D., 2010. History-matching flow simulations and time-lapse seismic data from the sleipner co2 plume. In: Geological Society of LondonGeological Society, London, Petroleum Geology Conference Series, 7, pp. 1171–1182.
Chadwick, R., Zweigel, P., Gregersen, U., Kirby, G., Holloway, S., Johannessen, P., 2004. Geological reservoir characterization of a CO_2 storage site: the Utsira Sand, Sleipner, northern North Sea. Energy, 29(9-10):1371–1381. 6th International Conference on Greenhouse Gas Control Technologies.
Chadwick, R., Williams, G., Williams, J., Noy, D., 2012. Measuring pressure performance of a large saline aquifer during industrial-scale CO_2 injection: the Utsira Sand, Norwegian North Sea. Int. J. Greenh. Gas Control. 10, 374–388.
Coléou, T., Allo, F., Bornard, R., Hamman, J., Caldwell, D., 2005. Petrophysical seismic inversion. SEG Technical Program Expanded Abstracts 2005. Society of Exploration Geophysicists, pp. 1355–1358.
Colombo, D., Rovetta, D., 2018. Coupling strategies in multiparameter geophysical joint inversion. Geophys. J. Int. 215 (2), 1171–1184.
Commer, M., Doetsch, J., Dafflon, B., Wu, Y., Daley, T.M., Hubbard, S.S., 2016. Time-lapse 3-d electrical resistance tomography inversion for crosswell monitoring of dissolved and supercritical co2 flow at two field sites: escatawpa and cranfield, mississippi, usa. Int. J. Greenh. Gas Control. 49, 297–311.
Davis, T.L., Landrø, M., Wilson, M., 2019. Geophysics and Geosequestration. Cambridge University Press.
De Barros, L., Dietrich, M., Valette, B., 2010. Full waveform inversion of seismic waves reflected in a stratified porous medium. Geophys. J. Int. 182 (3), 1543–1556.
de Figueiredo, L.P., Grana, D., Roisenberg, M., Rodrigues, B.B., 2019a. Gaussian mixture markov chain monte carlo method for linear seismic inversion. Geophysics 84 (3), R463–R476.
de Figueiredo, L.P., Grana, D., Roisenberg, M., Rodrigues, B.B., 2019b. Multimodal markov chain monte carlo method for nonlinear petrophysical seismic inversion. Geophysics 84 (5), M1–M13.
Dean, M., Tucker, O., 2017. A risk-based framework for measurement, monitoring and verification (MMV) of the Goldeneye storage complex for the Peterhead CCS project, UK. Int. J. Greenh. Gas Control. 61, 1–15.
Dell'Aversana, P., 2014. Integrated Geophysical Models. EAGE Publications bv, HOUTEN The Netherlands.
Dinh, H.N., Van der Baan, M., 2019. A grid-search approach for 4d pressure-saturation discrimination. Geophysics 84 (4), IM47–IM62.
Domenico, S.N., 1976. Effect of brine-gas mixture on velocity in an unconsolidated sand reservoir. Geophysics 41, 882–894.
Doyen, P., 2007. Seismic Reservoir Characterization: An Earth Modelling Perspective, 2. EAGE publications, Houten, p. 255.
Duffet, C., Sinoquet, D., 2006. Quantifying uncertainties on the solution model of seismic tomography. Inverse Probl. 22 (2).
Dupuy, B., Asnaashari, A., Brossier, R., Garambois, S., Metivier, L., Ribodetti, A., Virieux, J., 2016a. A downscaling strategy from FWI to microscale reservoir properties from high-resolution images. Lead. Edge 35 (2), 146–150.
Dupuy, B., Garambois, S., Virieux, J., 2016b. Estimation of rock physics properties from seismic attributes - Part 1: strategy and sensitivity analysis. Geophysics 81 (3), 35–53.
Dupuy, B., Romdhane, A., Eliasson, P., Querendez, E., Yan, H., Torres, V.A., Ghaderi, A., 2017. Quantitative seismic characterization of co2 at the sleipner storage site, north sea. Interpretation 5 (4), SS23–SS42.
Dupuy, B., Nordmann, P.-L., Romdhane, A., Eliasson, P., 2019. Bayesian rock physics inversion for CO_2 storage monitoring. Fourth EAGE Conference on Petroleum Geostatistics.
Dutta, A.J., Odé, H., 1979. Attenuation and dispersion of compressional waves in fluid-filled porous rocks with partial gas saturation (White model)-Part I: biot theory. Geophysics 44 (11), 1777–1788.
EC, 2011. Implementation of Directive 2009/31/EC on the Geological Storage of Carbon Dioxide: Guidance Document 1 – CO_2 Storage Life Cycle Risk Management Framework. ISBN-13978-92-79-19833-5. Technical report, EC.
Eiken, O., 2019. Twenty years of monitoring co2 injection at sleipner. In: Davis, T.L., Landro, M., Wilson, M. (Eds.), Geophysics and Geosequestration, pp. 209–234.
Eiken, O., Ringrose, P., Hermanrud, C., Nazarian, B., Torp, T.A., Høier, L., 2011. Lessons learned from 14 years of CCS operations: Sleipner, In Salah and Snøhvit. Energy Procedia 4, 5541–5548.
Eliasson, P., Romdhane, A., 2017. Uncertainty Quantification in Waveform-based Imaging Methods - A Sleipner CO_2 Monitoring Study. Energy Procedia. In press.
Evensen, G., 2009. The ensemble Kalman filter for combined state and parameter estimation. IEEE Control. Syst. Mag. 29 (3), 83–104.
Falcon-Suarez, I., Papageorgiou, G., Chadwick, A., North, L., Best, A.I., Chapman, M., 2018. CO_2-brine flow-through on an Utsira Sand core sample: experimental and modelling. Implications for the Sleipner storage field. Int. J. Greenh. Gas Control. 68, 236–246.
Fang, Z., Da Silva, C., Kuske, R., Herrmann, F.J., 2018. Uncertainty quantification for inverse problems with weak partial-differential-equation constraints. Geophysics 83 (6), R629–R647.
Fjeldstad, T., Grana, D., 2018. Joint probabilistic petrophysics-seismic inversion based on Gaussian mixture and Markov chain prior models. Geophysics 83 (1), R31–R42.
Furre, A.-K., Kiær, A., Eiken, O., 2015. CO_2-induced seismic time shifts at Sleipner. Interpretation 3 (3), SS23–SS35.
Furre, A.-K., Eiken, O., Alnes, H., Vevatne, J.N., Kiær, A.F., 2017. 20 years of monitoring CO_2 injection at Sleipner. Energy Procedia 114, 3916–3926.
Furre, A.-K., Meneguolo, R., Ringrose, P., Kassold, S., 2019. Building confidence in ccs: from sleipner to the northern lights project. First Break. 37 (7), 83–89.
Gassmann, F., 1951. Über die elastizität poröser medien. Vierteljahrsschrift der Naturforschenden Gesellschaft in Zurich 96, 1–23.
Ghaderi, A., Landrø, M., 2009. Estimation of thickness and velocity changes of injected carbon dioxide layers from prestack time-lapse seismic data. Geophysics 74 (2), O17–O28.
Ghosh, R., Sen, M.K., Vedanti, N., 2015. Quantitative interpretation of CO_2 plume from Sleipner (North Sea),using post-stack inversion and rock physics modeling. Int. J. Greenh. Gas Control. 32, 147–158.
Giraud, J., Ogarko, V., Lindsay, M., Pakyuz-Charrier, E., Jessell, M., Martin, R., 2019. Sensitivity of constrained joint inversions to geological and petrophysical input data uncertainties with posterior geological analysis. Geophys. J. Int. 218 (1), 666–688.
Glubokovskikh, S., Pevzner, R., Gunning, J., Dance, T., Shulakova, V., Popik, D., Popik, S., Bagheri, M., Gurevich, B., 2020. How well can time-lapse seismic characterize a small co2 leakage into a saline aquifer: Co2crc otway 2c experiment (victoria, australia). Int. J. Greenh. Gas Control. 92, 102854.
Grana, D., 2016. Bayesian linearized rock-physics inversion. Geophysics 81 (6), D625–D641.
Grana, D., Fjeldstad, T., Omre, H., 2017. Bayesian gaussian mixture linear inversion for geophysical inverse problems. Math. Geosci. 49 (4), 493–515.
Grude, S., Landrø, M., Osdal, B., 2013. Time-lapse pressure–saturation discrimination for CO_2 storage at the snøhvit field. Int. J. Greenh. Gas Control. 19, 369–378.
Grude, S., Landrø, M., Dvorkin, J., 2014. Pressure effects caused by CO_2 injection in the Tubåen Fm., the Snøhvit field. Int. J. Greenh. Gas Control. 27, 178–187.
Hansen, O., Gilding, D., Nazarian, B., Osdal, B., Ringrose, P., Kristoffersen, J.-B., Eiken, O., Hansen, H., 2013. Snøhvit: the history of injecting and storing 1Mt CO_2 in the fluvial Tubåen Fm. Energy Procedia 37, 3565–3567.
IPCC, 2005. In: Metz, B., Davidson, O., de Coninck, H.C., Loos, M., Meyer, L.A. (Eds.), Intergovernmental Panel on Climate Change Special Report on Carbon Capture and Storage. Technical Report, Prepared by Working Group III of the Intergovernmental Panel on Climate Change. Cambridge University Press, Cambridge, United Kingdom and New York, NY, USA, p. 442.
Jullum, M., Kolbjørnsen, O., 2016. A Gaussian-based framework for local Bayesian inversion of geophysical data to rock properties. Geophysics 81 (3), R75–R87.
Landrø, M., 2001. Discrimination between pressure and fluid saturation changes from time-lapse seismic data. Geophysics 66 (3), 836–844.
Lindeberg, E., 2013. Calculation of Thermodynamic Properties of CO_2, CH_4, H_2O and Their Mixtures Also Including Salt With the Excel Macro "CO_2 Thermodynamics'. SINTEF report.
Mavko, G., Mukerji, T., 1995. Seismic pore space compressibility and Gassmann's relation. Geophysics 60 (6), 1743–1749.
Mavko, G., Mukerji, T., Dvorkin, J., 2009. The Rocks Physics Handbooks, Tools for Seismic Analysis in Porous Media, second edition. Cambridge University Press, Cambridge, UK.
Mindlin, R.D., 1949. Compliance of elastic bodies in contact. J. Appl. Mech. 16, 259–268.
Morency, C., Luo, Y., Tromp, J., 2009. Finite-frequency kernels for wave propagation in porous media based upon adjoint methods. Geophys. J. Int. 179, 1148–1168.
Papageorgiou, G., Amalokwu, K., Chapman, M., 2016. Theoretical derivation of a brie-like fluid mixing law. Geophys. Prospect. 64 (4), 1048–1053.
Papageorgiou, G., Falcon-Suarez, I., Chapman, M., Best, A., 2018. Pressure-varying CO_2 distribution affects the ultrasonic velocities of synthetic sandstones. Int. J. Greenh. Gas Control. 74, 1–8.
Park, J., Fawad, M., Viken, I., Aker, E., Bjørnarå, T.I., 2013. CSEM sensitivity study for Sleipner CO_2-injection monitoring. Energy Procedia 37, 4199–4206. GHGT-11.
Pawar, R.J., Bromhal, G.S., Carey, J.W., Foxall, W., Korre, A., Ringrose, P.S., Tucker, O., Watson, M.N., White, J.A., 2015. Recent advances in risk assessment and risk management of geologic CO_2 storage. Int. J. Greenh. Gas Control. 40, 292–311.
Pride, S., 2005. *Hydrogeophysics*, chapter relationships between seismic and hydrological properties. Water Science and Technology Library. Springer, The Netherlands, pp. 253–284.

Pride, S., Berryman, J., Harris, J., 2004. Seismic attenuation due to wave-induced flow. J. Geophys. Res. 109 (B01201), 1–19.
Pride, S.R., Berryman, J.G., Commer, M., Nakagawa, S., Newman, G.A., Vasco, D.W., 2017. Changes in geophysical properties caused by fluid injection into porous rocks: analytical models. Geophys. Prospect.
Queißer, M., Singh, S.C., 2013. Full waveform inversion in the time lapse mode applied to CO_2 storage at Sleipner. Geophys. Prospect. 61 (3), 537–555.
Ringrose, P.S., Meckel, T.A., 2019. Maturing global CO_2 storage resources on offshore continental margins to achieve 2DS emissions reductions. Sci. Rep. 9 (1), 1–10.
Roach, L.A., White, D., 2018. Evolution of a deep co2 plume from time-lapse seismic imaging at the aquistore storage site, saskatchewan, canada. Int. J. Greenh. Gas Control. 74, 79–86.
Romdhane, A., Querendez, E., 2014. CO_2 characterization at the Sleipner field with full waveform inversion: application to synthetic and real data. Energy Procedia 63, 4358–4365.
Rubino, J.G., Velis, D.R., Sacchi, M.D., 2011. Numerical analysis of wave-induced fluid flow effects on seismic data: application to monitoring of CO_2 storage at the Sleipner field. J. Geophys. Res. 116.
Sambridge, M.S., 1999. Geophysical inversion with a neighbourhood algorithm - II. Appraising the ensemble. Geophys. J. Int. 138, 727–746.
Sayers, C., Kachanov, M., 1995. Microcrack-induced elastic wave anisotropy of brittle rocks. J. Geophys. Res. Solid Earth 100 (B3), 4149–4156.
Shapiro, S., 2003. Elastic piezosensitivity of porous and fractured rocks. Geophysics 68 (2), 482–486.
Shapiro, S.A., Kaselow, A., 2005. Porosity and elastic anisotropy of rocks under tectonic stress and pore-pressure changes. Geophysics.
Span, R., Wagner, W., 1996. A new equation of state for carbon dioxide covering the fluid region from the triple-point temperature to 1100 K at pressures up to 800 MPa. J. Phys. Chem. Ref. Data 25 (6), 1509–1596.
Subagjo, I., Dupuy, B., Park, J., Romdhane, A., Querendez, E., Stovas, A., 2018. Joint rock physics inversion of seismic and electromagnetic data for CO_2 monitoring at Sleipner. 24th European Meeting of Environmental and Engineering Geophysics.
Tarantola, A., 2005. Inverse Problem Theory and Methods for Model Parameter Estimation. Society for Industrial and Applied Mathematics, Philadelphia.
Trinh, P.-T., Brossier, R., Métivier, L., Tavard, L., Virieux, J., 2018. Efficient time-domain 3d elastic and viscoelastic full-waveform inversion using a spectral-element method on flexible cartesian-based mesh. Geophysics 84 (1), R75–R97.
Vasco, D., Alfi, M., Hosseini, S.A., Zhang, R., Daley, T., Ajo-Franklin, J.B., Hovorka, S.D., 2019. The seismic response to injected carbon dioxide: comparing observations to estimates based upon fluid flow modeling. J. Geophys. Res. Solid Earth.
Verdon, J.P., Kendall, J.-M., Stork, A.L., Chadwick, R.A., White, D.J., Bissell, R.C., 2013. Comparison of geomechanical deformation induced by megatonne-scale CO_2 storage at Sleipner, Weyburn, and In Salah. Proc. Natl. Acad. Sci. 110 (30), E2762–E2771.
Virieux, J., Operto, S., 2009. An overview of full waveform inversion in exploration geophysics. Geophysics 74 (6), WCC1–WCC26.
Walton, K., 1987. The effective elastic moduli of a random packing of spheres. J. Mech. Phys. Solids 35, 213–226.
Wang, Z., Harbert, W.P., Dilmore, R.M., Huang, L., 2018. Modeling of time-lapse seismic monitoring using co2 leakage simulations for a model co2 storage site with realistic geology: application in assessment of early leak-detection capabilities. Int. J. Greenh. Gas Control. 76, 39–52.
Watson, F., Andersen, O., Nilsen, H., Dupuy, B., Romdhane, A., Eliasson, P., 2019. Combining monitoring data and flow simulations for improved CO_2 storage security. TCCS-10 Proceedings, Trondheim (Norway).
White, J.E., 1975. Computed seismic speeds and attenuation in rocks with partial gas saturation. Geophysics 40 (2), 224–232.
Williams, G., Chadwick, A., 2012. Quantitative seismic analysis of a thin layer of CO_2 in the sleipner injection plume. Geophysics 77 (6), R245–R256.
Wollner, U., Dvorkin, J., 2018. Effective bulk modulus of the pore fluid at patchy saturation. Geophys. Prospect. 66 (7), 1372–1383.
Yan, H., Dupuy, B., Romdhane, A., Arntsen, B., 2019. CO_2 saturation estimates at Sleipner (North Sea) from seismic tomography and rock physics inversion. Geophys. Prospect. 67, 1055–1071.
Zhu, H., Li, S., Fomel, S., Stadler, G., Ghattas, O., 2016. A bayesian approach to estimate uncertainty for full-waveform inversion using a priori information from depth migration. Geophysics 81 (5), R307–R323.